# Déformation et anisotropie du manteau lithosphérique sous un rift mature

Le rift Est-Africain est l'un des principaux rifts actifs de la planète. Il offre la possibilité d'étudier le rifting à différents stades de maturité, de l'initiation jusqu'à l'accrétion océanique. Si des études ont apportées des contraintes importantes sur la déformation de surface et le magmatisme durant le rifting, ainsi que le rôle des panaches mantelliques (e.g. Biggs et al., 2011; Corti, 2008; Ebinger et al., 1993; Stewart et Rogers, 1996), peu de choses sont connues sur la manière dont le manteau accommode la déformation durant le rifting. La présence de magmas à petite échelle peut diminuer de façon significative la viscosité du manteau (Hirth and Kohlstedt, 2003; Kohlstedt and Zimmerman, 1996; Kohlstedt et al., 2000; Zimmerman and Kohlstedt, 2004). Or, la partie éthiopienne du rift Est Africain a été soumise à plusieurs épisodes magmatiques importants. La formation rapide du plateau magmatique Ethiopien il y a 30 Ma (Ebinger, 1993; Georges et al., 1998; Hofman et al., 1997) a précédé un second épisode volcanique et de début de l'extension au Miocène (Ebinger et al., 1993; Hendrie et al. 1994; Morley et al. 1992). Enfin, la région enregistre un dernier épisode volcanique Plio-Pléistocène, se traduisant sous la forme de cônes et de fissures volcaniques au cœur de la vallée du rift (Bonini et al., 2005; Ebinger et al., 1993; Furman, 2007; Shinjo et al., 2011).

Le travail présenté dans ce chapitre repose sur l'analyse de 25 xénolites mantelliques (20 péridotites, 5 pyroxénites) du rift Est-Africain au Sud de Mega, en bordure Sud du plateau éthiopien. Cette étude est basée sur la caractérisation des microstructures et des OPRs des xénolites éthiopiens, ainsi que le calcul de leurs propriétés sismiques. Elle vise à mieux comprendre les relations entre déformation et percolation de fluides et magmas durant le rifting.

Les péridotites du Sud de Mega présentent des microstructures homogènes, suggérant que ces roches n'enregistrent probablement pas de variations spatiales ou temporelles des conditions de déformation. Contrairement à ce qui a précédemment été rapporté par Bedini et al. (1997), nous n'observons pas de variations significatives des microstructures en fonction du type de métasomatisme. La variation de l'espacement entre sous-joints dans les

porphyroclastes d'olivine, ainsi que la polygonisation variable des néoblastes d'olivine, suggèrent une déformation suivie par un recuit variable. Les OPRs de l'olivine de type orthorhombique indiquent une déformation par fluage-dislocation avec activation du système de glissement [100] (010). La présence de clinopyroxène et d'orthopyroxène suggère une cristallisation secondaire, probablement associée à l'épisode métasomatique identifié par Bedini et al. (1997). Les OPRs mesurées dans l'orthopyroxène et parfois dans le clinopyroxène, ainsi que la cohérence généralement observée entre les OPRs de l'olivine et de l'orthopyroxène, indiquent un épisode métasomatique pré- à syn-cinématique.

L'anisotropie azimutale maximale des ondes P varie entre 3.1 et 12.3%, tandis que l'anisotropie de polarisation maximale des ondes S est comprise entre 2.9 et 8.3%. De telles anisotropies ne peuvent expliquer à elles seules les déphasages des ondes SKS mesurées au niveau du rift Ethiopien et du rift Kenyan. Les microstructures et les relations entre magmas et percolation dans les péridotites éthiopiennes sont différentes de celles observées dans les xénolites de la Divergence Nord-Tanzanienne ou du Nord Kenya. La comparaison de ces données indique que, bien que la percolation de magmas dans le manteau lithosphérique durant le rifting soit commune, son timing par rapport à la déformation varie.

# Deformation and anisotropy of the lithospheric mantle beneath a mature rift: constraints from mantle xenoliths from Southern Mega, SE Ethiopia

Virginie Baptiste, Andréa Tommasi, and Alain Vauchez

*Géosciences Montpellier, Université Montpellier 2 & CNRS, CC 60, Place E. Bataillon, 34095 Montpellier cedex 5, France.*

*Running title: Deformation of the lithospheric mantle beneath a mature rift*

(*) corresponding author: virginie.baptiste@gm.univ-montp2.fr;
Phone: +33 467144912
Fax: +33 467143603

## 1. Introduction

The East African rift is great natural laboratory, which allows studying continental rifting at variable degree of maturity, from its initiation to oceanic accretion. Over the past years, studies have brought important constraints on surface deformation and magmatism during rifting, as well as on the role of mantle plumes (e.g. Biggs et al., 2011; Corti, 2008; Ebinger et al., 1993; Stewart et Rogers, 1996). Despite this, little is known about how the lithospheric mantle accommodate rifting deformation through time. Many studies point out the major role of magmas during rifting initiation and formation. Buck (2006), for instance, proposed that dyke intrusions might help initiating the deformation within the strong continental lithosphere. This hypothesis is supported by seismic anisotropy studies, which suggest the presence of oriented melt pockets in the crust and the mantle within the rift axis in Ethiopia and in Afar (Bastow et al., 2010; Hammond et al., 2014). At a larger scale, body-wave tomography images a broad and deep low velocity anomaly beneath the Ethiopian Plateau and the eastern branch of the rift system in Kenya and Tanzania, that have been proposed to be linked to the African Superplume (Nyblade, 2011). The presence of magma at a smaller scale may significantly decrease mantle viscosity (Hirth and Kohlstedt, 2003; Kohlstedt and Zimmerman, 1996; Kohlstedt et al., 2000; Zimmerman and Kohlstedt, 2004). Reaction with melts or fluids may as well reduce mantle strength through crystallization of weaker phases, grain size reduction, and phase mixing (e.g., Dijkstra et al. 2002; Soustelle et al. 2010).

In Ethiopia, the rapid formation of the magmatic Plateau during a plume-related peak volcanism at 30 Ma (Ebinger, 1993; Georges et al., 1998; Hofman et al., 1997) preceded continental extension initiation and a later volcanic episode in the Miocene (Ebinger et al., 1993; Hendrie et al. 1994; Morley et al. 1992). The Ethiopian branch of the East African Rift, the main Ethiopian rift, is therefore an ideal location to study the way the lithospheric mantle accommodated the rifting deformation in a mature rift and the role of magmatism in this process.

In the present study, we explore the relation between deformation and melt percolation in a suite of mantle xenoliths from the southern end of the main Ethiopian rift (South of Mega, Sidamo region). Based on their crystallographic preferred orientations and mineralogical compositions, we also estimate their seismic anisotropy and compare it to seismic anisotropy data performed in the area.

## 2. Geological background

*2.1 Geological setting*

The East African rift is one of the most active rifts on Earth. It extends over more than 4000 km, from the Afar triple junction to the Gulf of Mozambique, and splits into two branches around the Tanzanian craton. The Eastern branch and the main Ethiopian rift of the East African rift overlap in the Turkana Depression, a 300 km wide system of extensional basins (Shinjo et al., 2011), where the earliest traces of volcanic activity (45 Ma) in the East African rift system were found (Ebinger et al., 1993, Georges et al., 1998). Extension in the main Ethiopian rift started in South Ethiopia at ~25-20 Ma (Ebinger et al., 1993; Hoffman et al., 1997; Kieffer et al., 2004; Woldegabriel et al., 1991), through the thick Ethiopian plateau, which formed from a peak volcanic activity at 31-30 Ma. The region also records two later, lower volumes, volcanic episodes: one during the Miocene (19-11 Ma) dominated by alkaline basalts and trachytes, and another during the Plio-Pleistocene, occurring as fissural lavas and cinder cones within the rift axis (Bonini et al., 2005; Ebinger et al., 1993; Furman, 2007; Shinjo et al., 2011).

Seismic studies have investigated the structure of the Ethiopian rift. Joint inversion of Rayleigh wave group velocities and receiver functions indicate lithospheric thicknesses of 80-90 km beneath the Ethiopian Plateau (Dugda et al, 2007). In the lithospheric mantle, maximum S-waves velocities of 4.3 km/s and 4.1-4.2 km/s are measured beneath the Ethiopian Plateau and the main Ethiopian rift, respectively (Dugda et al, 2007). Based on 1D conductive thermal model, Dugda et al. (2007) suggested that a plume model could explain this structure, provided that the lithosphere was thinned by ~30-50 km, above a plume during the flood basalt volcanism at 30 Ma, and the warm material stayed beneath the lithosphere since then. Beneath the Ethiopian Plateau, body-wave tomographies also image a 500 km wide and 400 km thick anomaly at ~100-300 km depth, interpreted as the upper mantle continuation of the African Superplume (Bastow et al., 2008, Benoit et al., 2006). Within the main Ethiopian rift, SKS studies report coherent rift-parallel polarization of the fast S-wave (Gashawbeza et al., 2004; Kendall et al., 2005), but variable delay times (0.5-1.7s: Gashawbeza et al., 2004, 1-3 s: Kendall et al., 2005). Variations in splitting parameters and increasing amount of splitting above regions of recent volcanism support the idea of an anisotropic signal dominated by oriented melt pockets (Ayele et al., 2004; Kendall et al., 2005). However, beneath the Ethiopian plateau, the measured anisotropy may be related to a pre-existing fabric frozen in the lithosphere (Gashawbeza et al., 2004; Hammond et al., 2014). Surface waves and SKS studies report the presence of a ~100 km thick anisotropic upper

layer (Bastow et al., 2010; Hammond et al., 2010; Sicilia et al., 2008), possibly caused by a fossil fabric (Sicilia et al., 2008), which locally contains oriented melt pockets (Bastow et al., 2010; Hammond, 2014; Sicilia et al., 2008). A more recent SKS study shows the existence of two anisotropic layers (Hammond et al., 2014): an upper layer with variable polarization directions in the Ethiopian plateau and the main Ethiopian rift, and lower anisotropic layer with a consistent NE-SW orientation that could be attributed to flow from the African Superplume.

In the Sidamo region (South Mega, SE Ethiopia), on the southern border of the Ethiopian plateau and the southern end of the Ethiopian rift, lava flows and pyroclastic rocks with basanitic to nephelinitic compositions erupted in the late Pleistocene, carrying mantle xenoliths (Morten et al., 1992; Bedini et al., 1997). The present study focuses on twenty-five mantle xenoliths from this region (Fig. 1).

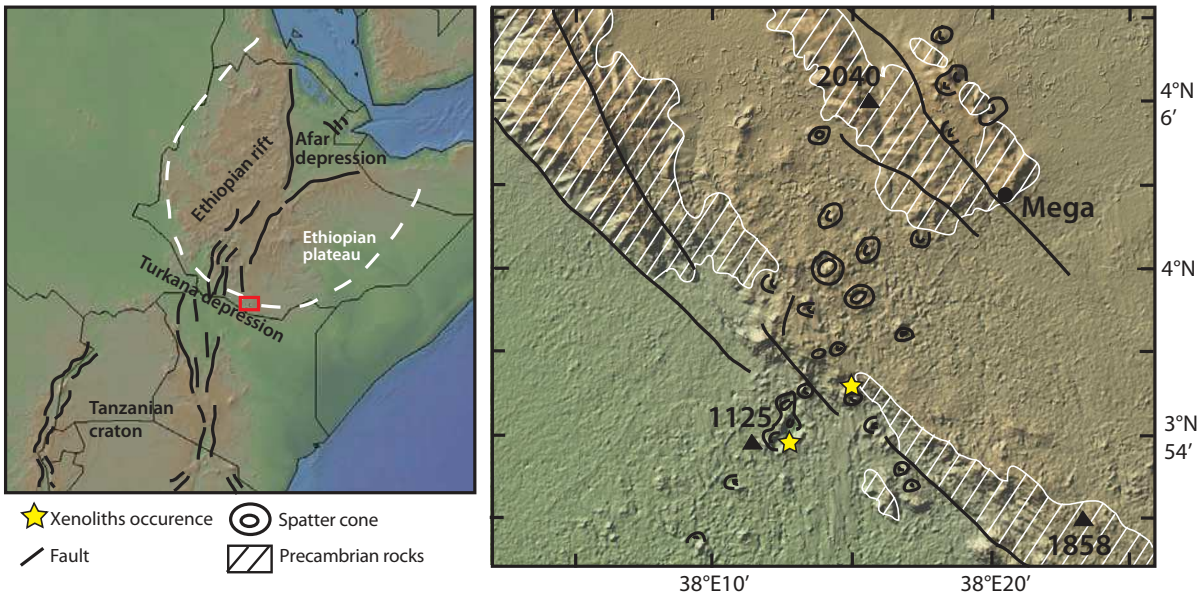


Fig. 1: Digital topographic map (http://www.geomapapp.org, topography data from Ryan et al., 2009) showing the East African rift and the xenolith localities studied here. Location of the Precambrien rocks, spatter cones, and faults near Mega were reported as in Morten et al. (1992).

### *2.2 Sample set: geochemical background*

The geochemical composition of the studied mantle xenoliths has been previously studied in detail (Bedini, 1994; Bedini et al., 1997; Bedini et al., 1999; Lorand et al., 2003). Bedini et al. (1997) showed that beneath south Mega, the lithospheric mantle was infiltrated by asthenospheric magmas linked to a mantle plume. During their upward migration, these magmas reacted with the surrounding peridotite, which progressively modified their

composition, generating different types of metasomatism along the percolated column and through time (Bedini et al., 1997). Bedini et al. (1997) indeed identified two geochemical groups among the peridotites from south Mega: (1) The less recrystallized samples (or "deformed"), strongly enriched in LILE, with negative anomalies of the HFSE and sometimes apatite-bearing, (2) The more recrystallized samples (or "granular"), depleted or slightly enriched in LILE and devoided of significant HFSE anomaly. The geochemical characteristics of "deformed" peridotites were interpreted as the result of interaction with small fractions of LILE-enriched melts saturated in Ti-oxides, while "granular" peridotites are believed to have re-equilibrated with high fractions of basaltic melts (Bedini et al., 1997). In deformed peridotites, PGE abundances and sulphides modal compositions suggest interaction with volatile-rich small melt fractions (Lorand et al., 2003), while in granular peridotites, re-equilibration with OIB-like melts in high porosity zones at the bottom of the lithosphere is likely.

Because our observations and interpretations on sample microstructures are significantly different than that of Bedini et al. (1997), we will refer in the following to "deformed" peridotites as "metasomatism 1" (M1) peridotites and to granular peridotites as "metasomatism 2" (M2) peridotites.

## 3. Methods

### *3.1 Electron-backscattered diffraction (EBSD)*

The crystallographic preferred orientations (CPO) of olivine, pyroxenes, garnet and spinel were measured at the SEM-EBSD facility at Geosciences Montpellier by indexation of electron back-scattered diffraction (EBSD) patterns produced by interaction of an incident electron beam with a carefully polished thin section tilted at 70° to the electron beam. Measurements were performed in a JEOL JSM 5600 scanning electron microscope using an acceleration voltage of 17 kV and a working distance of 23 mm. Maps covering almost entirely each thin section were obtained using steps between 100 and 30 μm, depending on grain size. Indexation rates ranged between 70 and 90% depending of the mineral. Orthopyroxene and clinopyroxene were seldom misindexed for one another. Careful post-acquisition data treatment by comparing EBSD maps and microscopic observations was performed to reduce inaccurate mineral determination and misindexation due to olivine pseudosymmetry. Grain sizes and modal compositions were also obtained from EBSD maps.

Crystal-preferred orientation data is displayed in pole figures, presented as lower hemisphere stereographic projections. To avoid over-representation of large grains, data were

reduced to one average crystallographic orientation per grain. When the foliation and lineation could be identified, the orientation of the main crystallographic directions: [100], [010] and [001] for olivine and pyroxenes, was plotted relatively to the principal axes of the deformation ellipsoid X, Y, and Z. Because the foliation and lineation could not be identified in coarse-grained samples, thin sections were cut in random orientations. To allow comparison between different samples, we rotated the CPO of randomly oriented samples into a common orientation, in which the maximum concentration of olivine [100] and [010] axes are parallel to the E–W and the N–S directions of the pole figure, respectively.

To better describe the olivine CPO symmetry, we calculated the dimensionless BA index (Mainprice et al., 2014) defined as:

$$BAindex = \frac{1}{2}\left(2-\left(\frac{P010}{G010+P010}\right)-\left(\frac{G100}{G100+P100}\right)\right) \quad (1)$$

Where P and G are indexes used to characterize the shape of the distribution (P for Point and G for Girdle; Vollmer, 1990) of the olivine principal axes ([100], [010] and [001]); these indexes were calculated from the eigenvalues of the normalized orientation matrix as P=λ1-λ3 and G=2(λ2-λ3), calculated using the MTEX texture analysis Matlab toolbox (Hielscher and Schaeben, 2008; Mainprice et al., 2011). The BA index allows a more precise classification of the olivine CPO symmetry into 3 types: axial-[010] (BA index<0.35), orthorhombic (0.35<BA index<0.65), and axial-[100] (BA index>0.65).

The strength of the fabric was quantified using the dimensionless J-index, which is the volume-averaged integral of squared orientation densities defined by:

$$J = \int f(g)^2 dg \quad (2)$$

where f(g) is the orientation distribution function (ODF) and $dg = d\varphi_1 d\varphi d\varphi_2 \sin\varphi\pi^2$. $\varphi_1$, $\varphi$, and $\varphi_2$ are the Euler angles, that define the rotations allowing for coincidence between the crystallographic and external reference frames. Natural peridotites classically show J-indexes between 2 and 20, with a peak at 8–10 (Ben Ismaïl and Mainprice, 1998; Tommasi et al., 2000). The J-index for each sample was calculated based on the mean orientation of each grain using the MTEX texture analysis Matlab toolbox.

*3.2 Seismic properties*

Seismic properties were calculated using the CPO of all major phases and their respective modal content estimated from EBSD maps (Mainprice, 1990). For olivine,

Table 1:

| Sample | Thin section name | Rock type | Apatite-bearing samples | Texture | Metasomatism type from Bedini et al. (1997) | Temperature[a] (°C) | Ol Mg# (%) | Opx Mg# (%) | Reference for mg# and T data | Modal compositions[b] (%) | | | | | Olivine CPO type | Olivine J-index | Olivine BA index | Density ($g.cm^{-3}$) | Max AVp (%) | Max AVs pol (%) | Max $AVS_1$ (%) | Max $AVS_2$ (%) |
|---|---|---|---|---|---|---|---|---|---|---|---|---|---|---|---|---|---|---|---|---|---|---|
| | | | | | | | | | | ol | opx | cpx | gt | sp | | | | | | | | |
| ET32 | ET32 | Lz | | CP | M2 | 1049 | 88.5 | 89.3 | Bedini, 1994 | 46 | 36 | 16 | 0 | 2 | ortho | 3.8 | 0.39 | 3.3676 | 3.1 | 3.9 | 2.6 | 2.8 |
| ET40 | ET40 | Lz | | CP | M2 | - | - | - | - | 62 | 21 | 15 | 0 | 2 | ortho | 3.1 | 0.71 | 3.3752 | 4.3 | 3.7 | 1.8 | 2.9 |
| ET41 | ET41 | Lz | x | CP | M1 | - | - | - | - | 78 | 14 | 7 | 0 | 1 | ortho | 3.9 | 0.42 | 3.3635 | 7.0 | 6.4 | 3.5 | 3.7 |
| ET46 | ET46 | Lz | x | CP | M1 | 1009 | 90.9 | 91.8 | Bedini, 1994 | 83 | 11 | 5 | 0 | 1 | ortho | 5.7 | 0.48 | 3.3656 | 10.5 | 6.6 | 3.8 | 5.8 |
| ET48 | ET48A | Lz | | CP | M2 | 942 | 89.5 | 89.8 | Bedini, 1994 | 52 | 26 | 20 | 0 | 2 | ortho | 3.0 | 0.75 | 3.3714 | 4.7 | 2.9 | 1.8 | 2.6 |
| | ET48B | Lz | | CP | M2 | | | | | 56 | 29 | 14 | 0 | 1 | ortho | 5.1 | 0.59 | 3.3542 | 5.4 | 4.9 | 2.5 | 2.9 |
| ET49 | ET49 | Hz | x | CP | M1 | 954 | 91.2 | 92.0 | Bedini, 1994 | 81 | 15 | 3 | 0 | 1 | ortho | 3.2 | 0.56 | 3.3642 | 6.8 | 4.9 | 2.4 | 3.5 |
| ET53 | ET53 | Lz | | CP | M2 | 969 | 90.2 | 90.9 | Bedini, 1994 | 72 | 16 | 11 | 0 | 1 | ortho | 4.7 | 0.69 | 3.3614 | 7.8 | 5.3 | 2.2 | 4.9 |
| ET54 | ET54 | Hz | x | CP | M1 | 901 | 91.5 | 92.2 | Bedini, 1994 | 84 | 12 | 4 | 0 | 0 | ortho | 7.8 | 0.62 | 3.3480 | 12.3 | 8.0 | 4.5 | 5.9 |
| ET63 | ET63 | Lz | | CP | M2 | - | - | - | - | 46 | 24 | 26 | 0 | 4 | ortho | 3.9 | 0.34 | 3.4054 | 3.8 | 3.0 | 2.3 | 1.6 |
| ET66 | ET66A | Lz | | CP* | M1 | - | - | - | - | 69 | 24 | 6 | 0 | 1 | ortho | 2.7 | 0.58 | 3.3439 | 5.6 | 3.6 | 1.6 | 3.4 |
| | ET66B | Hz | | CP* | M1 | - | - | - | - | 76 | 21 | 3 | 0 | 0 | ortho | 2.0 | 0.43 | 3.3695 | 4.9 | 3.5 | 1.6 | 2.4 |
| ET69 | ET69 | Lz | x | CP | M1 | 863 | 90.7 | 91.3 | Bedini, 1994 | 50 | 32 | 16 | 0 | 2 | axial-[010] to ortho | 4.9 | 0.45 | 3.3695 | 5.2 | 4.5 | 2.4 | 3.0 |
| ET70 | ET70A | Lz | | CP | M2 | - | - | - | - | 61 | 14 | 23 | 0 | 2 | ortho | 4.0 | 0.56 | 3.3584 | 5.5 | 4.4 | 2.3 | 3.0 |
| | ET70B | Lz | | CP | M2 | - | - | - | - | 53 | 30 | 15 | 0 | 2 | ortho | 4.9 | 0.51 | 3.3708 | 3.3 | 3.3 | 2.7 | 2.1 |
| ET73 | ET73 | Lz | | CP | M2 | - | - | - | - | 61 | 19 | 17 | 0 | 3 | axial-[010] | 5.5 | 0.49 | 3.3930 | 5.8 | 4.3 | 2.4 | 3.4 |
| ET74 | ET74A | Lz | | CP | M2 | 916 | 90.9 | 91.6 | Bedini, 1994 | 61 | 14 | 23 | 0 | 2 | ortho | 3.1 | 0.43 | 3.3764 | 6.5 | 4.2 | 2.2 | 3.1 |
| | ET74B | Lz | | CP | M2 | | | | | 64 | 16 | 19 | 0 | 1 | ortho | 5.0 | 0.53 | 3.3592 | 8.6 | 5.4 | 2.1 | 4.2 |
| ET76 | ET76 | Lz | | CP | M2 | 933 | 89.5 | 90.3 | Bedini, 1994 | 57 | 30 | 10 | 0 | 3 | ortho | 3.5 | 0.79 | 3.3895 | 5.2 | 4.0 | 1.6 | 3.4 |
| ET82 | ET82 | Lz | | CP | M2 | - | - | - | - | 62 | 20 | 17 | 0 | 1 | axial-[010] | 3.0 | 0.41 | 3.3578 | 4.1 | 3.7 | 2.4 | 2.7 |
| ET83 | ET83A | Hz | x | CP | M1 | - | - | - | - | 84 | 13 | 2 | 0 | 1 | axial-[010] to ortho | 5.7 | 0.58 | 3.3654 | 11.4 | 7.4 | 4.0 | 6.1 |
| | ET83B | Hz | x | CP | M1 | - | - | - | - | 72 | 25 | 2 | 0 | 1 | axial-[010] to ortho | 5.0 | 0.45 | 3.3595 | 7.3 | 5.7 | 2.4 | 3.6 |
| ET84 | ET84A | Hz | x | CP* | M1 | 830 | 92.1 | 92.7 | Bedini, 1994 | 86 | 11 | 3 | 0 | 0 | axial-[100] to ortho | 4.2 | 0.56 | 3.3488 | 7.4 | 5.4 | 2.1 | 4.3 |
| | ET84B | Hz | x | CP* | M1 | | | | | 76 | 22 | 1 | 0 | 1 | axial-[100] to ortho | 4.8 | 0.68 | 3.3613 | 8.8 | 6.9 | 3.2 | 5.4 |
| ET85 | ET85A | Lz | | CP | M1 | - | - | - | - | 85 | 10 | 5 | 0 | 0 | ortho | 6.4 | 0.49 | 3.3487 | 10.6 | 7.7 | 4.8 | 4.4 |
| | ET85B | Lz | | CP | M1 | - | - | - | - | 66 | 13 | 17 | 0 | 4 | ortho | 9.5 | 0.69 | 3.4133 | 6.4 | 5.7 | 3.6 | 3.6 |
| ET-VB1 | ET-VB1 | Hz | | CP* | - | - | - | - | - | 79 | 17 | 3 | 0 | 1 | ortho | 7.2 | 0.39 | 3.3632 | 12.2 | 8.3 | 5.8 | 5.3 |
| ET55 | ET55A | Wb | | CP | - | - | - | - | - | 0 | 36 | 64 | 0 | 0 | - | - | - | 3.3194 | 6.9 | 4.2 | 4.2 | 3.6 |
| | ET55B | Wb | | CP | - | - | - | - | - | 0 | 14 | 86 | 0 | 0 | - | - | - | 3.3241 | - | - | 10.6 | 12.3 |
| ET64B | ET64B | Wb | | G | - | - | - | - | - | 0 | 44 | 54 | 0 | 2 | - | - | - | 3.3530 | 4.8 | 3.4 | 2.4 | 1.8 |
| ET68 | ET68 | Cpx | | CP | - | - | - | - | - | 0 | 0 | 90 | 10 | 0 | - | - | - | 3.3753 | 12.8 | 9.8 | 8.5 | 8.5 |
| ET77 | ET77 | Wb | | CP | - | - | - | - | - | 0 | 42 | 58 | 0 | 0 | - | - | - | 3.3182 | 6.5 | 4.9 | 4.0 | 3.5 |
| ET81 | ET81 | Wb | | G | - | - | - | - | - | 0 | 36 | 53 | 10 | 1 | - | - | - | 3.3854 | 5.7 | 4.4 | 2.3 | 3.8 |

[a] Brey and Köhler (1990) thermometry;

[b] Modal compositions determined from EBSD maps;

* Samples bearing automorphic olivines;

Texture: CP= Coarse-porphyroclastic; G= Granular;

Metasomatism type from Bedini et al. (1997):M1= Deformed ; M2= Granular;

CPO types: ortho= orthorhombic, axial-[100], axial-[010], axial-[100] to orthorhombic, and axial-[010] to orthorhombic crystal-preferred orientations, see main text for details.

AVp: Vp azimuthal anisotropy; AVs: Vs azimuthal anisotropy; $AVs_1$: Fast Vs azimuthal anisotropy; $AVs_2$: Slow Vs azimuthal anisotropy; maximum values

orthopyroxene, clinopyroxene, garnet and spinel single-crystal elastic constant tensors at ambient conditions were used (Abramson et al., 1997; Chai et al., 1997a; Chai et al., 1997b; Collins and Brown, 1998; Hearmon, 1984). A Voigt-Reuss-Hill averaging was applied in all calculations. The seismic anisotropy parameters and the elastic constants of all samples are presented in Table 1 and online Supplementary Material 1, respectively.

*3.3 Thermometry*

The samples equilibrium temperature was calculated using the mineral compositions measured by Bedini (1994). The two pyroxenes Fe-Mg exchange geothermometer from Brey and Köhler (1990; uncertainty of ±50°C) was chosen. Since post-exsolution pyroxene compositions were used in the calculation, the equilibration temperatures are lower than the temperatures that would be obtained for "primary" pyroxene compositions. Primary equilibration temperatures were estimated by Bedini et al. (1997) for one peridotite of each group, by taking into account the volume of exsolutions in the orthopyroxene; they are of 1130°C (±10) and of 1210°C (±20) for a deformed and a granular peridotite, respectively.
However, the data on the exsolutions volume fraction and composition is not available for the other samples.

## 4. Results

*4.1 Modal compositions and equilibrium temperatures*

Because most of the xenoliths from Mega were entirely used during previous geochemical analysis (Bedini, 1994; Bedini et al., 1997; Bedini et al., 1999), we were able to obtain the thin sections of 25 xenoliths out of the originally larger sample set of Bedini (1994). In the present sample set, M1 peridotites are mainly harzburgites, while M2 peridotites are mainly lherzolites (Fig. 2 and Table 1). However, it has to be emphasized that the two groups included both harzburgites and lherzolites in the larger xenolith suite analysed by Bedini et al. (1997). In both M1 and M2 peridotites, orthopyroxene contents vary mainly between 10 and 35%. In M2 lherzolites, clinopyroxene content is highly variable, ranging between 10 and 26% (Table 1). In these rocks, the olivine content varies between 46 and 72%. In addition to these peridotites, we have also analyzed four websterites (three spinel-bearing and one garnet-bearing) and one garnet clinopyroxenite (Fig.2 and Table 1).
The M1 peridotites studied here display high olivine Mg# (Mg#: atomic Mg/(Fe+Mg)), ranging between 90.7 and 92.1% (Table 1). M2 peridotites tend to display lower olivine Mg#, varying between 88.5 and 90.9%. Equilibrium temperatures range between 830 and 1049°C

(Table 1). There is no systematic correlation between temperature and the geochemical group or the microstructure.

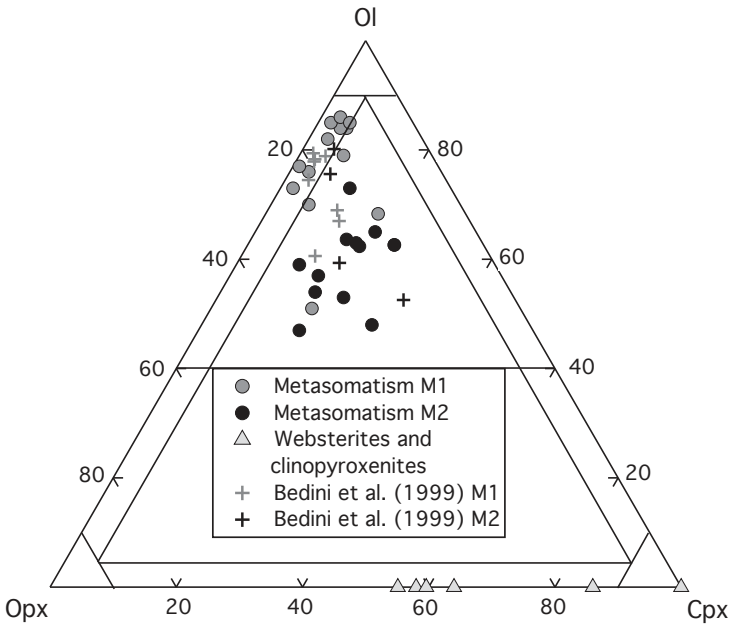


Fig. 2: Olivine:Orthopyroxene:Clinopyroxene modal ratios in the studied xenoliths as a function of the metasomatism type of Bedini et al. (1997) (M1= Deformed; M2= Granular), and rock type. Garnet and spinel were not considered for the construction of the ternary diagram; modal compositions derived from the EBSD maps were recalculated for a total of 100% of Olivine+Orthopyroxene+Clinopyroxene. Modal compositions in twelve samples from Mega reported by Bedini et al. (1999) are plotted for comparison.

*4.2 Microstructures*

The microstructural analysis of the peridotites from Mega reveals that there is no marked change in microstructures between M1 and M2 peridotites as previously reported by Bedini et al. (1997). Ethiopian peridotites have dominantly coarse-porphyroclastic microstructures (Fig. 3). They present plurimillimetric olivine porphyroclasts with well-defined subgrain boundaries. Smaller olivine neoblasts (~0.4- 3 mm) usually show fewer intracrystalline deformation features and tend to have more polygonal shapes, sometimes forming triple junctions. The subgrain boundary spacing and the frequency of triple junctions vary from a sample to another. For example, in sample ET48 (Fig. 3a), the subgrain boundaries in olivine porphyroclasts are closely-spaced and triple junctions are rare, whereas in sample ET53 (Fig. 3b), neoblasts commonly have polygonal boundaries, as well as some porphyroclasts.

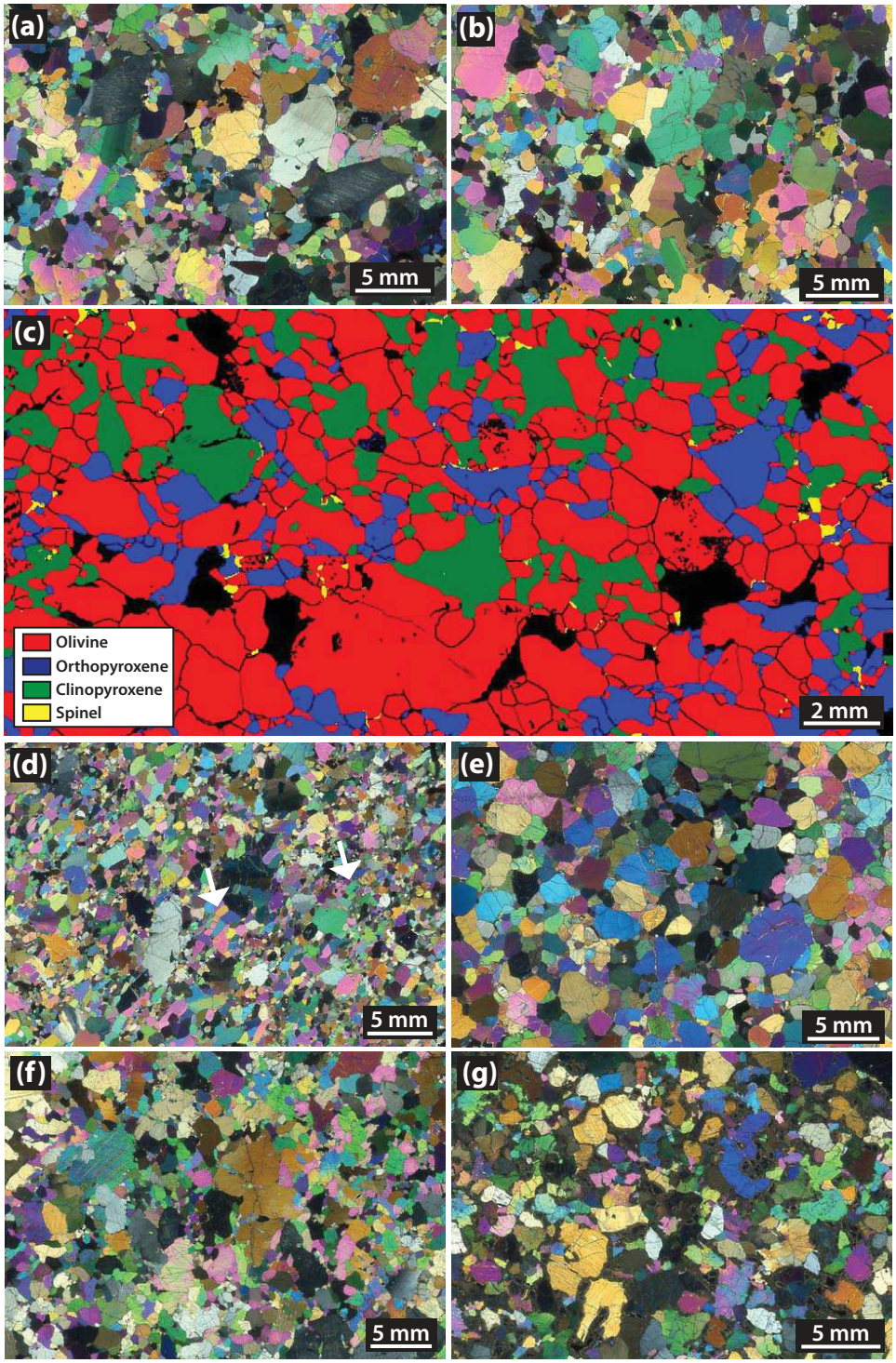


Fig. 3: Photomicrographs in plane-polarised light (a, b, d, e, f, g) and EBSD map (c) of: (a) coarse-porphyroclastic lherzolite ET48A, with large olivine porphyroclasts showing well- defined subgrain boundaries. Orthopyroxene porphyroclasts display kink bands and exsolutions. Olivine neoblasts free of internal deformation features are also present; (b) Coarse-porphyroclastic lherzolite ET53, showing olivine porphyroclasts and neoblasts that tends to have polygonal grain boundaries; (c) EBSD maps of the coarse-porphyroclastic lherzolite ET74B, where large orthopyroxene and clinopyroxene porphyroclasts are visible, as well as smaller, interstitial orthopyroxene and clinopyroxene grains; (d) Coarse- pophyroclastic lherzolite ET66A, where euhedral olivine tablets (arrows) can be found among the olivine neoblasts; (e) Granular websterite ET64 with plurimillimetric

orthopyroxene and clinopyroxene crystals with common polygonal grain boundaries; (f) Coarse-porphyroclastic websterite ET77, with large orthopyroxene and clinopyroxene crystals with well-defined undulose extinctions and exsolutions, as well as smaller pyroxene neoblasts devoid of intracrystalline deformation features; (g) Coarse-porphyroclastic websterite ET81, with interstitial garnet crystal partially kelyphitized.

In three samples (ET-VB1, ET66, and ET84), tabular olivines with polygonal boundaries and devoid of any intracrystalline deformation features can be observed (Fig. 3d). In five samples, olivine interpenetrating boundaries are present. Orthopyroxene porphyroclasts are plurimillimetric and anhedral (Fig. 3a-b). They often display intracrystalline deformation features, such as well-defined kink bands and undulose extinctions. In seventeen samples, they contain exsolutions. Large orthopyroxene crystals (~0.4-1cm) often contain olivine inclusions and interpenetrating olivine-orthopyroxene boundaries are common (Fig. 3a). Smaller orthopyroxene grains (0.7-3mm) are also present (Fig. 3c). They commonly display interstitial shapes and rarely contain subgrain boundaries. In most samples, isolated interstitial clinopyroxene grains (0.3-3mm) can be observed (Fig. 3c). Twelve samples show plurimillimetric and anhedral clinopyroxene porphyroclasts with rare subgrain boundaries. These grains often contain olivine inclusions. When present, spinel occurs as dark, irregularly shaped, millimetric to plurimillimetric grains. In sample ET85, plurimillimetric are concentrated in a smaller area and surrounded by very small olivine and clinopyroxene grains.

Websterites and clinopyroxenites microstructures range from granular (ET64, ET81) (Fig. 3e) to coarse-porphyroclastic (ET55, ET68, ET77; Fig. 3f). In the granular websterites, the plurimillimetric clinopyroxene and orthopyroxene crystals often display polygonal boundaries and exsolutions. In the porphyroclastic websterites, millimetric to centimetric anhedral porphyroclasts of clinopyroxene with exsolutions can be observed. They sometime exhibit undulose extinctions as well as kink bands. The millimetric neoblasts tend to display polygonal boundaries and are devoid of intracrystalline deformation features. In ET68 and ET81, garnet crystals are partially kelyphitized and millimetric to plurimillimetric (Fig. 3g). In ET81, it is present as small interstitial grains, while in ET68, it is enclosed both interstitial and enclosed within clinopyroxene.

*4.3 Crystallographic preferred orientations*

Peridotites from Ethiopia exhibit variable olivine CPO intensity, characterized by J-indexes ranging between 2.0 and 9.5, and dominantly orthorhombic patterns (Fig.4 and Table 1). There is no correlation between the olivine CPO symmetry and strength. There is also no

systematic variation in the olivine CPO among the two geochemical groups defined by Bedini et al. (1997)

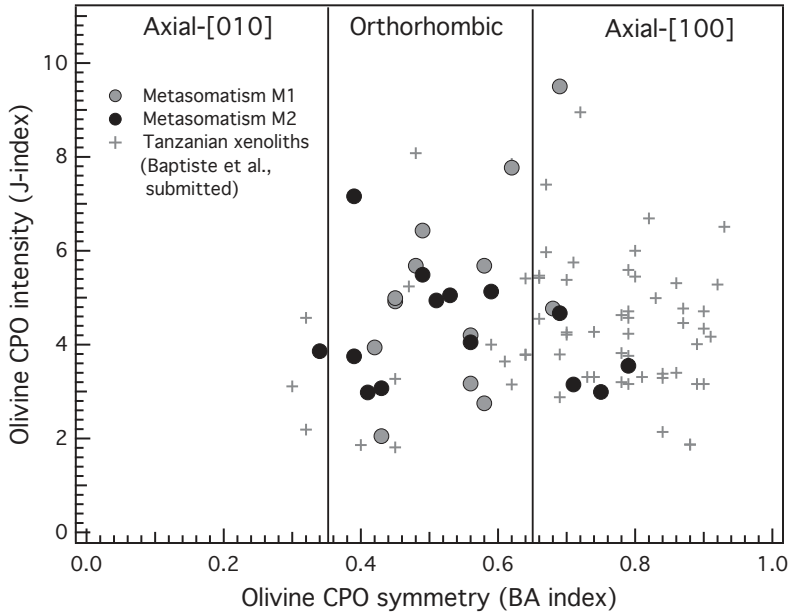


Fig. 4: Olivine CPO intensity (J-index) vs. symmetry (BA index) for all samples as a function of the metasomatism type.

The dominant olivine CPO patterns are characterized by point concentrations of the three crystallographic axis, with [100] usually showing the strongest concentration (Fig. 5). In two samples (ET73 and ET82), axial-[010] CPOs are observed. These patterns are characterized by a point concentration of [010] axes, and a girdle distribution of [100] and [001] normal to it. Sample ET83 shows an olivine CPO pattern intermediate between orthorhombic and axial-[010]. It is characterized by a point concentration of [010] and incomplete girdles of [100] and [001] axes. Finally, in sample ET84, a pattern intermediate between orthorhombic and axial-[100] is observed, with a point concentration of [100] axes and incomplete girdles of [010] and [001] axes.

Orthopyroxene CPO patterns are more dispersed than the olivine ones. They exhibit weak point concentrations of the three crystallographic axes. In most samples, orthopyroxene [100] and [001] maximum concentrations are parallel to olivine the [010] and [100] maximum concentrations, respectively. Clinopyroxene CPOs are still more dispersed than orthopyroxene CPOs. When a clinopyroxene CPO can be defined, it is correlated to the olivine and orthopyroxene CPOs, with clinopyroxene [001] being parallel to orthopyroxene [001] and olivine [100].

## PERIDOTITES: Metasomatism 1

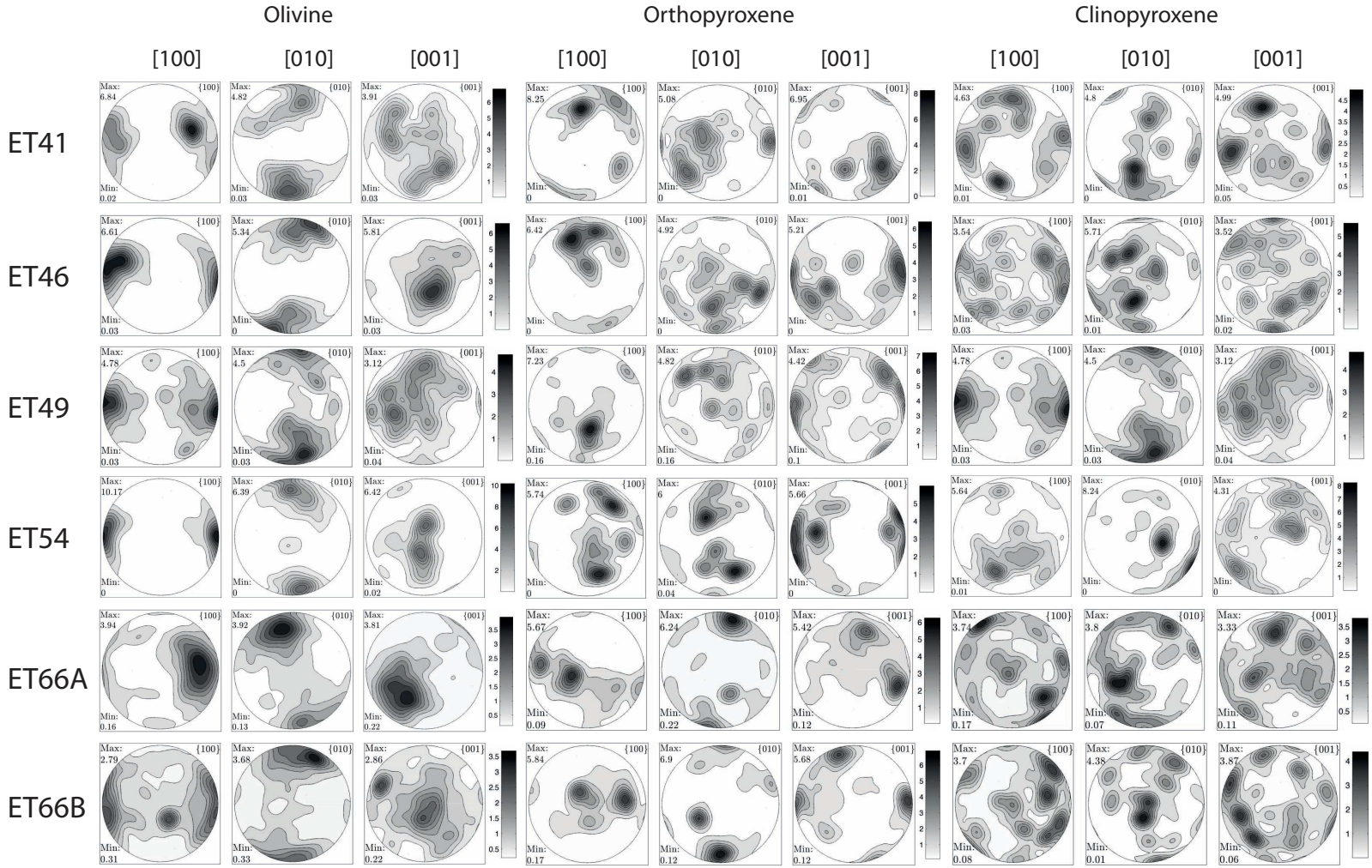


Fig. 5: Olivine, orthopyroxene, and clinopyroxene crystal preferred orientations (CPO) for all samples.

## PERIDOTITES: Metasomatism 1

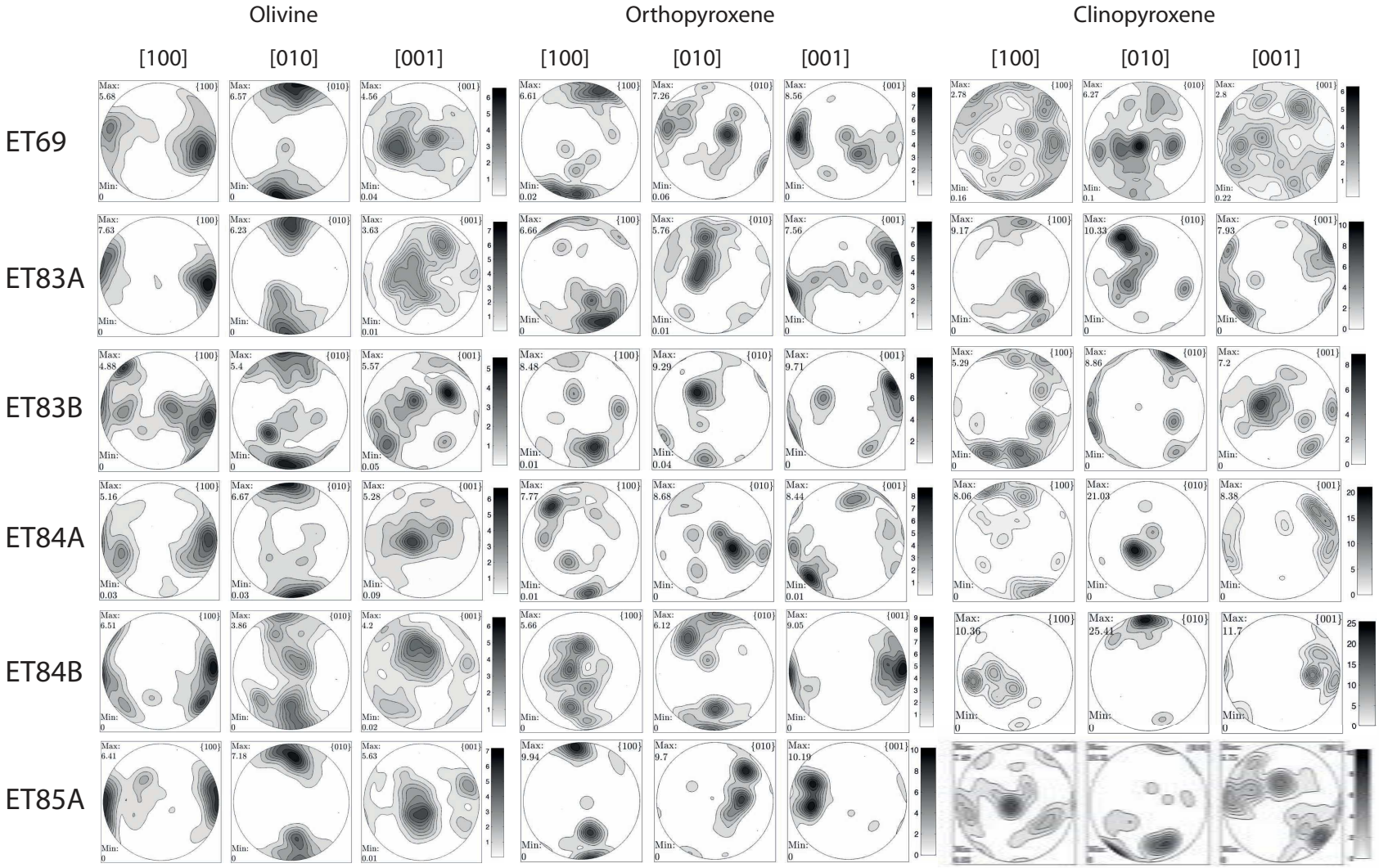


Fig. 5 (suite)

## METASOMATISM 2

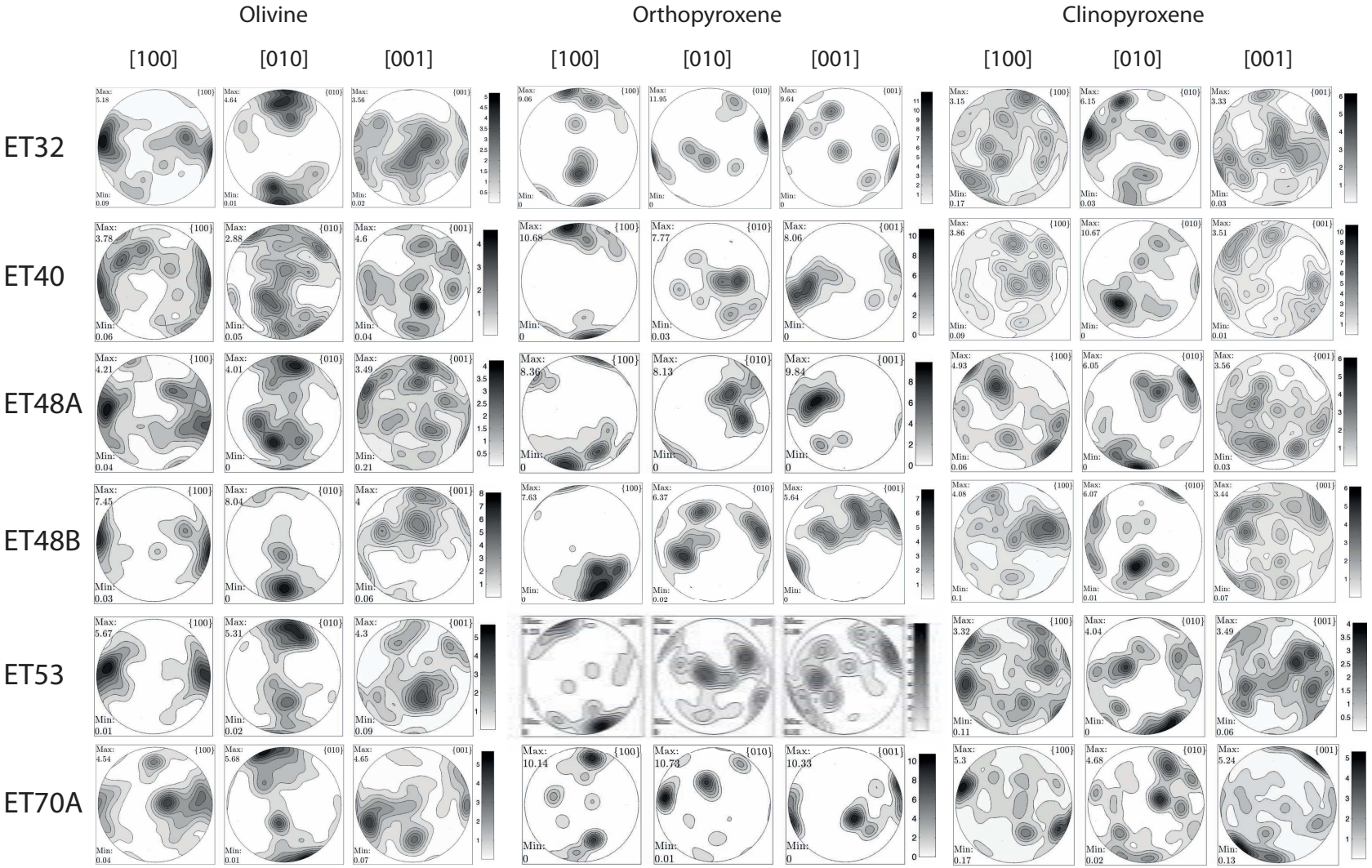


Fig. 5 (suite)

## PERIDOTITES: Metasomatism 2

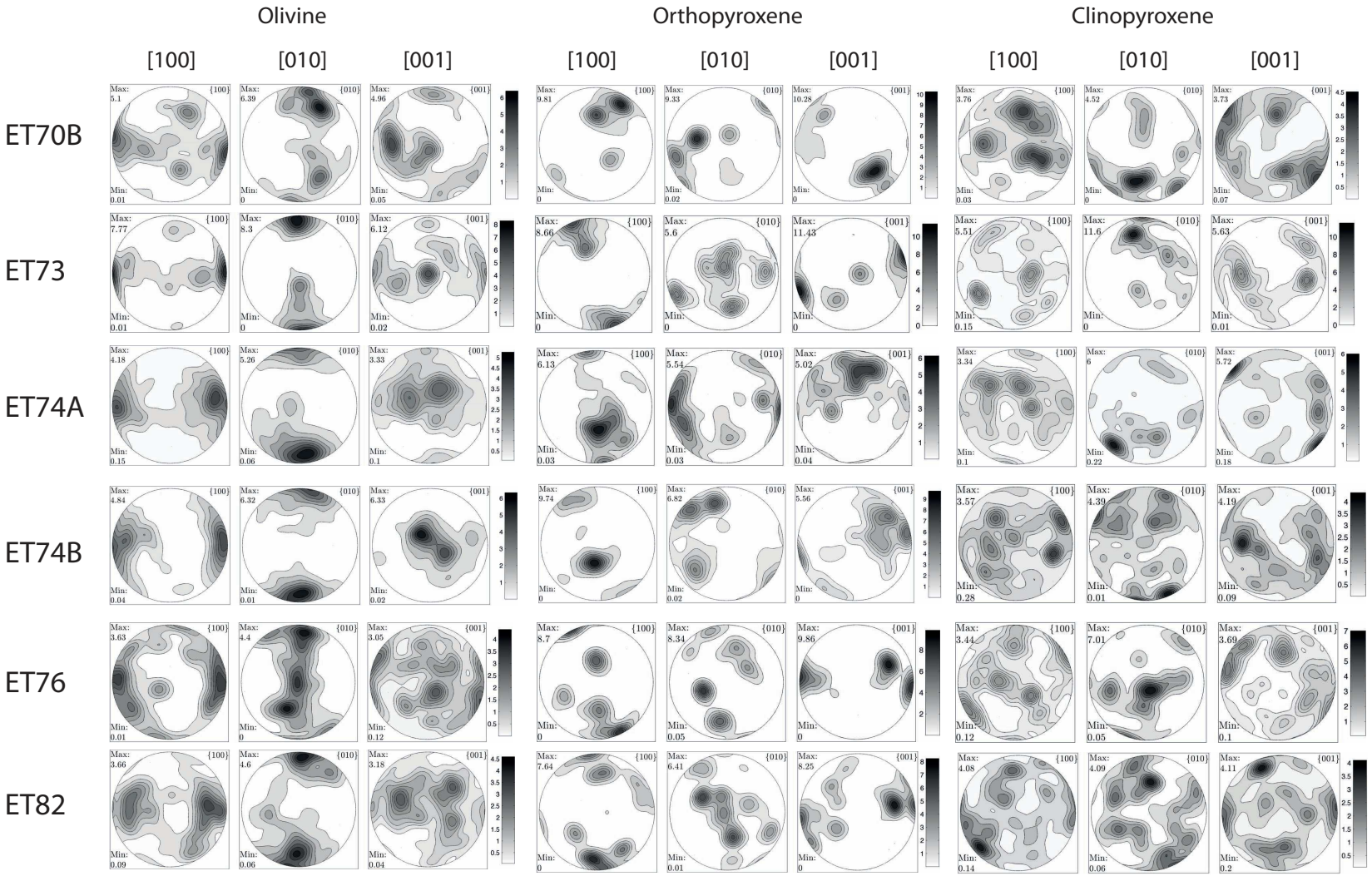


Fig. 5 (suite)

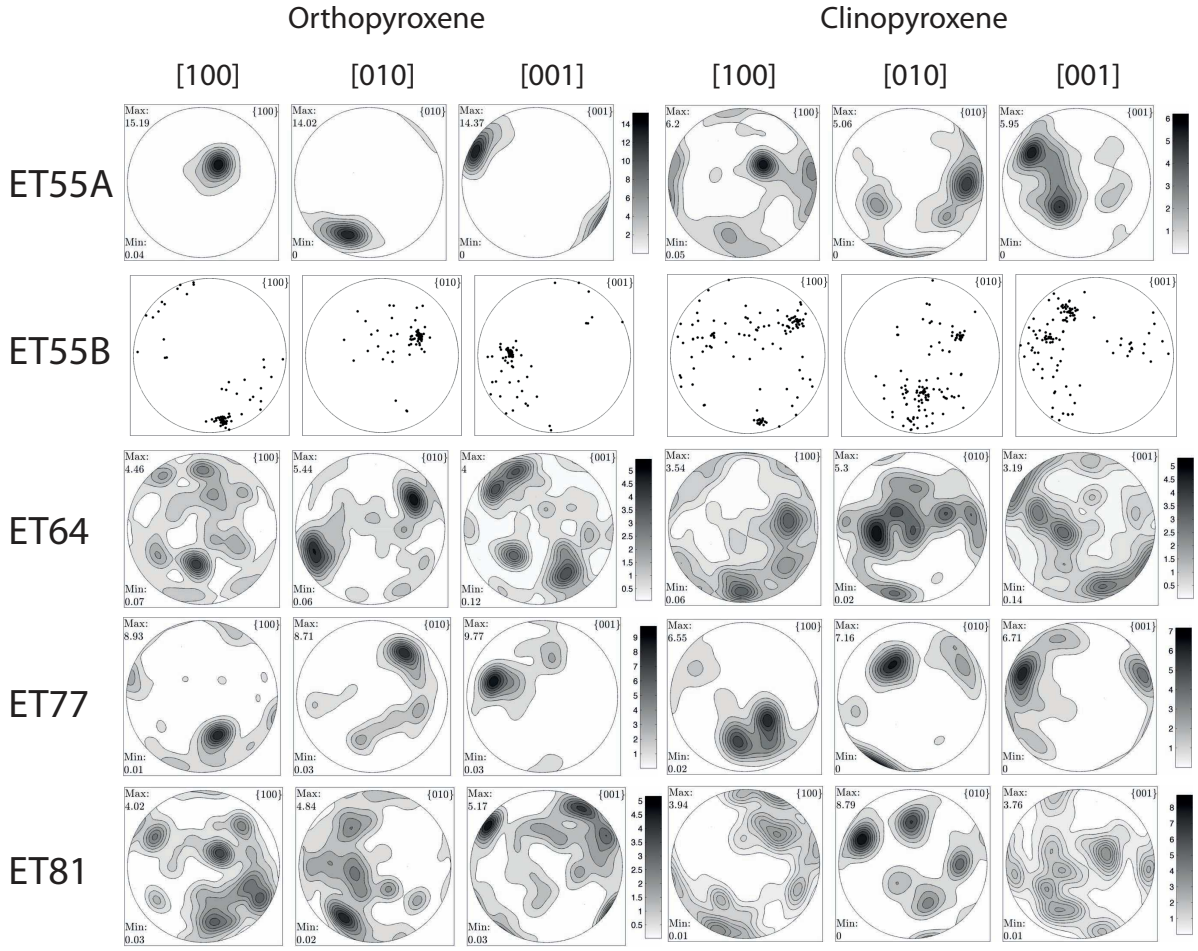
Orthopyroxene
Clinopyroxene
[100]
[010]
[001]
[100]
[010]
[001]
ET55A
ET55B
ET64
ET77
ET81

Fig. 5 (suite)

All pyroxenites show orthopyroxene and clinopyroxene CPO with a weak orthorhombic pattern. Only two samples (ET77 and ET81) have coherent orthopyroxene and clinopyroxene CPOs. In the thwo other websterites (ET55 and ET64), they are not correlated.

*4.4 Seismic properties*

All peridotites share a common seismic anisotropy pattern (Fig. 6). The P-waves propagation is the fastest close to the olivine [100] maximum and the slowest close to [010] maximum. S-waves azimuthal anisotropy is the highest close to the olivine [001] and the slowest for directions close to maximum concentration of olivine [100] axes. The slowest propagation of the S1-wave occurs for directions close to the olivine [010] maximum, while the fastest S1 propagation is in the plane containing the olivine [100] and [010] maxima, close to Y or at 45° to it. The slowest propagation directions of the slow S-wave ($S_2$) are in the plane containing the olivine [010] and [001] maxima. The fastest velocities of S2-waves are observed for directions close to the maximum concentration of olivine [100] axes. The highest $Vp/Vs_1$ ratio is also parallel to the olivine [100] maximum and the lowest Vp/Vs1 is observed for waves propagating normal to this direction.

Seismic anisotropy intensities for individual samples are highly variable (Fig. 7 and Table 1). Maximum P-waves anisotropies are comprised between 3.1 and 12.3%, while maximum S-waves polarization anisotropies range between 2.9 and 8.3 %. Both anisotropies show a positive correlation with olivine content (Fig. 7). Because pyroxenes and garnet are known to dilute the rock bulk anisotropy (Mainprice et al., 2000; Mainprice and Silver, 1993), the samples with higher olivine contents are generally more anisotropic.

Websterites and clinopyroxenites also show highly variable anisotropies. Maximum P-waves anisotropies range between 4.8 and 12.8%, while maximum S-waves polarization anisotropies are comprised between 4.2 and 9.8 %. In clinopyroxenite ET68 and websterite ET55, P-wave and $VS_2$ velocities are the fastest and $Vp/Vs_1$ ratios the highest parallel to the maximum concentration of clinopyroxene [001] axis and minimum at high angle to this direction, in a plane containing the [010] maximum. The S-waves polarization anisotropy pattern is more complex. S-waves polarization anisotropy tend to be maximum for directions close to the clinopyroxene [100] maximum concentration. In the other samples, P-wave and $VS_2$ velocities are fastest and $Vp/Vs_1$ ratios the highest parallel to the maximum concentration of orthopyroxene [001] axis and minimum at high angle to this direction, in a plane containing the orthopyroxene [100] maximum. S-waves polarization anisotropy maximum varies significantly from a sample to another.

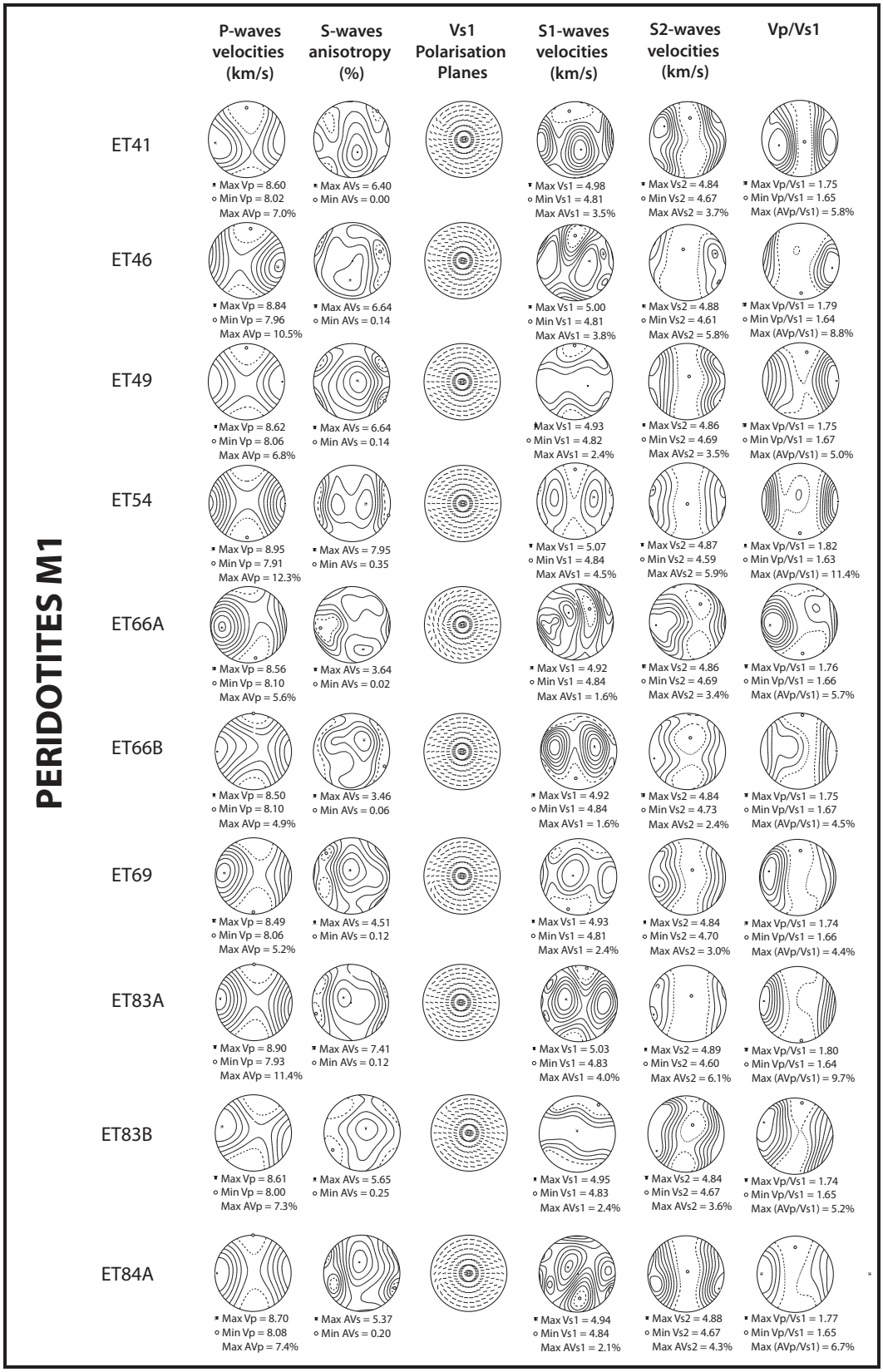


Fig. 6: Calculated seismic properties for all samples. From left to right are displayed the 3-D distributions of P-wave velocities ($V_p$), S-wave polarization anisotropy ($AV_s$) and the orientation of fast shear wave polarization plane, $S_1$ wave velocities ($VS_1$), $S_2$ wave velocities, $Vp/VS_1$ and $Vp/VS_2$ ratio. Black squares and white spots indicate maximum and minimum values, respectively.

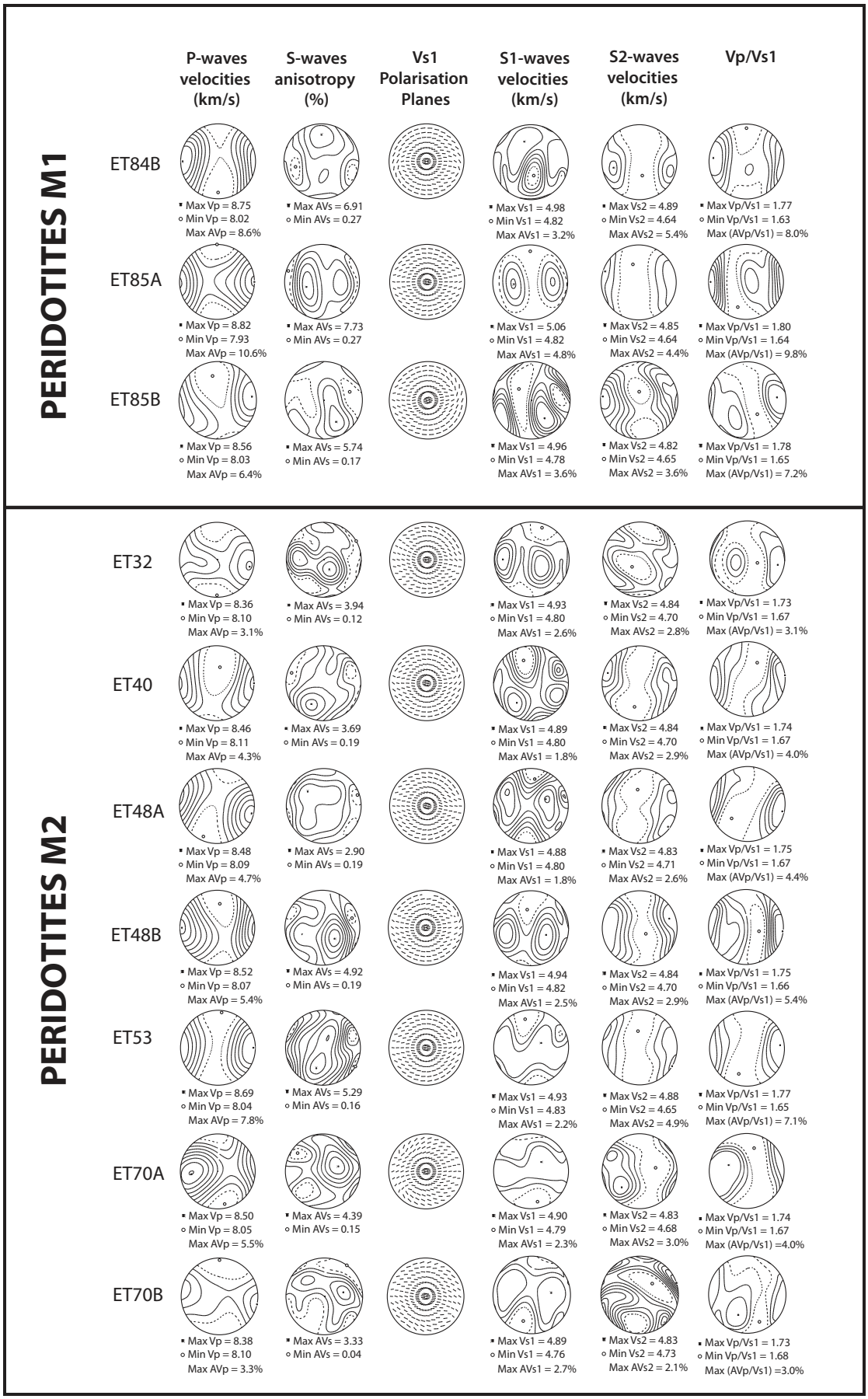
PERIDOTITES M1
P-waves velocities (km/s)
S-waves anisotropy (%)
Vs1 Polarisation Planes
S1-waves velocities (km/s)
S2-waves velocities (km/s)
Vp/Vs1
ET84B
▪ Max Vp = 8.75
◦ Min Vp = 8.02
Max AVp = 8.6%
▪ Max AVs = 6.91
◦ Min AVs = 0.27
▪ Max Vs1 = 4.98
◦ Min Vs1 = 4.82
Max AVs1 = 3.2%
▪ Max Vs2 = 4.89
◦ Min Vs2 = 4.64
Max AVs2 = 5.4%
▪ Max Vp/Vs1 = 1.77
◦ Min Vp/Vs1 = 1.63
Max (AVp/Vs1) = 8.0%
ET85A
▪ Max Vp = 8.82
◦ Min Vp = 7.93
Max AVp = 10.6%
▪ Max AVs = 7.73
◦ Min AVs = 0.27
▪ Max Vs1 = 5.06
◦ Min Vs1 = 4.82
Max AVs1 = 4.8%
▪ Max Vs2 = 4.85
◦ Min Vs2 = 4.64
Max AVs2 = 4.4%
▪ Max Vp/Vs1 = 1.80
◦ Min Vp/Vs1 = 1.64
Max (AVp/Vs1) = 9.8%
ET85B
▪ Max Vp = 8.56
◦ Min Vp = 8.03
Max AVp = 6.4%
▪ Max AVs = 5.74
◦ Min AVs = 0.17
▪ Max Vs1 = 4.96
◦ Min Vs1 = 4.78
Max AVs1 = 3.6%
▪ Max Vs2 = 4.82
◦ Min Vs2 = 4.65
Max AVs2 = 3.6%
▪ Max Vp/Vs1 = 1.78
◦ Min Vp/Vs1 = 1.65
Max (AVp/Vs1) = 7.2%
PERIDOTITES M2
ET32
▪ Max Vp = 8.36
◦ Min Vp = 8.10
Max AVp = 3.1%
▪ Max AVs = 3.94
◦ Min AVs = 0.12
▪ Max Vs1 = 4.93
◦ Min Vs1 = 4.80
Max AVs1 = 2.6%
▪ Max Vs2 = 4.84
◦ Min Vs2 = 4.70
Max AVs2 = 2.8%
▪ Max Vp/Vs1 = 1.73
◦ Min Vp/Vs1 = 1.67
Max (AVp/Vs1) = 3.1%
ET40
▪ Max Vp = 8.46
◦ Min Vp = 8.11
Max AVp = 4.3%
▪ Max AVs = 3.69
◦ Min AVs = 0.19
▪ Max Vs1 = 4.89
◦ Min Vs1 = 4.80
Max AVs1 = 1.8%
▪ Max Vs2 = 4.84
◦ Min Vs2 = 4.70
Max AVs2 = 2.9%
▪ Max Vp/Vs1 = 1.74
◦ Min Vp/Vs1 = 1.67
Max (AVp/Vs1) = 4.0%
ET48A
▪ Max Vp = 8.48
◦ Min Vp = 8.09
Max AVp = 4.7%
▪ Max AVs = 2.90
◦ Min AVs = 0.19
▪ Max Vs1 = 4.88
◦ Min Vs1 = 4.80
Max AVs1 = 1.8%
▪ Max Vs2 = 4.83
◦ Min Vs2 = 4.71
Max AVs2 = 2.6%
▪ Max Vp/Vs1 = 1.75
◦ Min Vp/Vs1 = 1.67
Max (AVp/Vs1) = 4.4%
ET48B
▪ Max Vp = 8.52
◦ Min Vp = 8.07
Max AVp = 5.4%
▪ Max AVs = 4.92
◦ Min AVs = 0.19
▪ Max Vs1 = 4.94
◦ Min Vs1 = 4.82
Max AVs1 = 2.5%
▪ Max Vs2 = 4.84
◦ Min Vs2 = 4.70
Max AVs2 = 2.9%
▪ Max Vp/Vs1 = 1.75
◦ Min Vp/Vs1 = 1.66
Max (AVp/Vs1) = 5.4%
ET53
▪ Max Vp = 8.69
◦ Min Vp = 8.04
Max AVp = 7.8%
▪ Max AVs = 5.29
◦ Min AVs = 0.16
▪ Max Vs1 = 4.93
◦ Min Vs1 = 4.83
Max AVs1 = 2.2%
▪ Max Vs2 = 4.88
◦ Min Vs2 = 4.65
Max AVs2 = 4.9%
▪ Max Vp/Vs1 = 1.77
◦ Min Vp/Vs1 = 1.65
Max (AVp/Vs1) = 7.1%
ET70A
▪ Max Vp = 8.50
◦ Min Vp = 8.05
Max AVp = 5.5%
▪ Max AVs = 4.39
◦ Min AVs = 0.15
▪ Max Vs1 = 4.90
◦ Min Vs1 = 4.79
Max AVs1 = 2.3%
▪ Max Vs2 = 4.83
◦ Min Vs2 = 4.68
Max AVs2 = 3.0%
▪ Max Vp/Vs1 = 1.74
◦ Min Vp/Vs1 = 1.67
Max (AVp/Vs1) =4.0%
ET70B
▪ Max Vp = 8.38
◦ Min Vp = 8.10
Max AVp = 3.3%
▪ Max AVs = 3.33
◦ Min AVs = 0.04
▪ Max Vs1 = 4.89
◦ Min Vs1 = 4.76
Max AVs1 = 2.7%
▪ Max Vs2 = 4.83
◦ Min Vs2 = 4.73
Max AVs2 = 2.1%
▪ Max Vp/Vs1 = 1.73
◦ Min Vp/Vs1 = 1.68
Max (AVp/Vs1) =3.0%

Fig. 6 (suite)

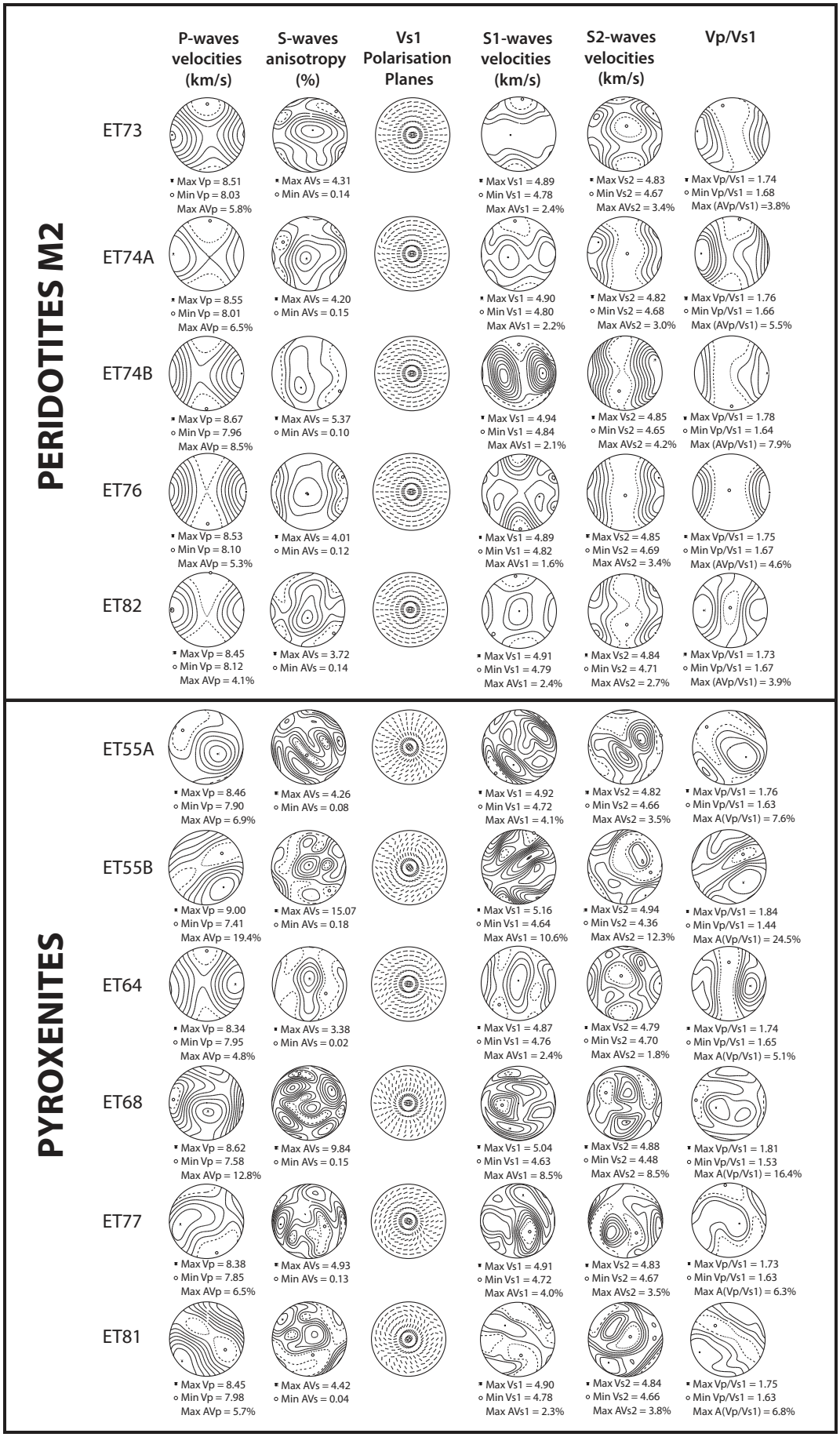
PERIDOTITES M2
PYROXENITES
P-waves velocities (km/s)
S-waves anisotropy (%)
Vs1 Polarisation Planes
S1-waves velocities (km/s)
S2-waves velocities (km/s)
Vp/Vs1
ET73
▪ Max Vp = 8.51
◦ Min Vp = 8.03
Max AVp = 5.8%
▪ Max AVs = 4.31
◦ Min AVs = 0.14
▪ Max Vs1 = 4.89
◦ Min Vs1 = 4.78
Max AVs1 = 2.4%
▪ Max Vs2 = 4.83
◦ Min Vs2 = 4.67
Max AVs2 = 3.4%
▪ Max Vp/Vs1 = 1.74
◦ Min Vp/Vs1 = 1.68
Max (AVp/Vs1) =3.8%
ET74A
▪ Max Vp = 8.55
◦ Min Vp = 8.01
Max AVp = 6.5%
▪ Max AVs = 4.20
◦ Min AVs = 0.15
▪ Max Vs1 = 4.90
◦ Min Vs1 = 4.80
Max AVs1 = 2.2%
▪ Max Vs2 = 4.82
◦ Min Vs2 = 4.68
Max AVs2 = 3.0%
▪ Max Vp/Vs1 = 1.76
◦ Min Vp/Vs1 = 1.66
Max (AVp/Vs1) = 5.5%
ET74B
▪ Max Vp = 8.67
◦ Min Vp = 7.96
Max AVp = 8.5%
▪ Max AVs = 5.37
◦ Min AVs = 0.10
▪ Max Vs1 = 4.94
◦ Min Vs1 = 4.84
Max AVs1 = 2.1%
▪ Max Vs2 = 4.85
◦ Min Vs2 = 4.65
Max AVs2 = 4.2%
▪ Max Vp/Vs1 = 1.78
◦ Min Vp/Vs1 = 1.64
Max (AVp/Vs1) = 7.9%
ET76
▪ Max Vp = 8.53
◦ Min Vp = 8.10
Max AVp = 5.3%
▪ Max AVs = 4.01
◦ Min AVs = 0.12
▪ Max Vs1 = 4.89
◦ Min Vs1 = 4.82
Max AVs1 = 1.6%
▪ Max Vs2 = 4.85
◦ Min Vs2 = 4.69
Max AVs2 = 3.4%
▪ Max Vp/Vs1 = 1.75
◦ Min Vp/Vs1 = 1.67
Max (AVp/Vs1) = 4.6%
ET82
▪ Max Vp = 8.45
◦ Min Vp = 8.12
Max AVp = 4.1%
▪ Max AVs = 3.72
◦ Min AVs = 0.14
▪ Max Vs1 = 4.91
◦ Min Vs1 = 4.79
Max AVs1 = 2.4%
▪ Max Vs2 = 4.84
◦ Min Vs2 = 4.71
Max AVs2 = 2.7%
▪ Max Vp/Vs1 = 1.73
◦ Min Vp/Vs1 = 1.67
Max (AVp/Vs1) = 3.9%
ET55A
▪ Max Vp = 8.46
◦ Min Vp = 7.90
Max AVp = 6.9%
▪ Max AVs = 4.26
◦ Min AVs = 0.08
▪ Max Vs1 = 4.92
◦ Min Vs1 = 4.72
Max AVs1 = 4.1%
▪ Max Vs2 = 4.82
◦ Min Vs2 = 4.66
Max AVs2 = 3.5%
▪ Max Vp/Vs1 = 1.76
◦ Min Vp/Vs1 = 1.63
Max A(Vp/Vs1) = 7.6%
ET55B
▪ Max Vp = 9.00
◦ Min Vp = 7.41
Max AVp = 19.4%
▪ Max AVs = 15.07
◦ Min AVs = 0.18
▪ Max Vs1 = 5.16
◦ Min Vs1 = 4.64
Max AVs1 = 10.6%
▪ Max Vs2 = 4.94
◦ Min Vs2 = 4.36
Max AVs2 = 12.3%
▪ Max Vp/Vs1 = 1.84
◦ Min Vp/Vs1 = 1.44
Max A(Vp/Vs1) = 24.5%
ET64
▪ Max Vp = 8.34
◦ Min Vp = 7.95
Max AVp = 4.8%
▪ Max AVs = 3.38
◦ Min AVs = 0.02
▪ Max Vs1 = 4.87
◦ Min Vs1 = 4.76
Max AVs1 = 2.4%
▪ Max Vs2 = 4.79
◦ Min Vs2 = 4.70
Max AVs2 = 1.8%
▪ Max Vp/Vs1 = 1.74
◦ Min Vp/Vs1 = 1.65
Max A(Vp/Vs1) = 5.1%
ET68
▪ Max Vp = 8.62
◦ Min Vp = 7.58
Max AVp = 12.8%
▪ Max AVs = 9.84
◦ Min AVs = 0.15
▪ Max Vs1 = 5.04
◦ Min Vs1 = 4.63
Max AVs1 = 8.5%
▪ Max Vs2 = 4.88
◦ Min Vs2 = 4.48
Max AVs2 = 8.5%
▪ Max Vp/Vs1 = 1.81
◦ Min Vp/Vs1 = 1.53
Max A(Vp/Vs1) = 16.4%
ET77
▪ Max Vp = 8.38
◦ Min Vp = 7.85
Max AVp = 6.5%
▪ Max AVs = 4.93
◦ Min AVs = 0.13
▪ Max Vs1 = 4.91
◦ Min Vs1 = 4.72
Max AVs1 = 4.0%
▪ Max Vs2 = 4.83
◦ Min Vs2 = 4.67
Max AVs2 = 3.5%
▪ Max Vp/Vs1 = 1.73
◦ Min Vp/Vs1 = 1.63
Max A(Vp/Vs1) = 6.3%
ET81
▪ Max Vp = 8.45
◦ Min Vp = 7.98
Max AVp = 5.7%
▪ Max AVs = 4.42
◦ Min AVs = 0.04
▪ Max Vs1 = 4.90
◦ Min Vs1 = 4.78
Max AVs1 = 2.3%
▪ Max Vs2 = 4.84
◦ Min Vs2 = 4.66
Max AVs2 = 3.8%
▪ Max Vp/Vs1 = 1.75
◦ Min Vp/Vs1 = 1.63
Max A(Vp/Vs1) = 6.8%

Fig. 6 (suite)

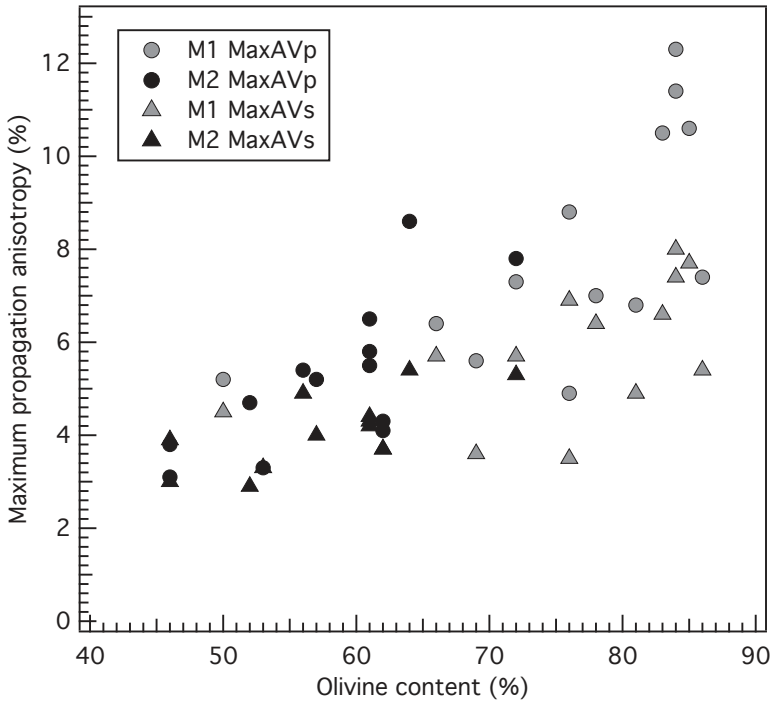


Fig. 7: Dependence of the maximum P- and S-waves anisotropy (AVp, AVs) on the olivine content.

## 5. Discussion

*5.1 Deformation history of the mantle peridotites*

All peridotites from south of Mega exhibit coarse-porphyroclastic microstructures, with evidence for plastic deformation by dislocation creep, followed by some static recrystallization. The homogeneity in microstructures and grain size suggest that these rocks record no major temporal or spatial variations of deformation conditions. However, the slight variations in subgrain boundaries spacing in olivine porphyroclasts and in grain boundary polygonization variable annealing degrees. The preservation of well-defined intracrystalline deformation features in olivine porphyroclasts suggests, however, that the time span between deformation and xenolith extraction was short enough to prevent complete annealing of the deformation microstructures. Common exsolutions in orthopyroxenes suggest post-kinematic cooling. Temperatures in the two samples devoid of exsolutions are high (959°C and 1009°C in ET53 and ET46, respectively). There is no clear correlation between temperature and microstructures or the geochemical group.

The well-defined olivine CPOs indicate that dislocation creep was the main deformation process. Most samples have orthorhombic olivine CPO patterns, coherent with deformation by pure or simple shear with dominant activation of (010)[100] slip system under

high temperature, low pressure and anhydrous conditions (e.g. Nicolas and Poirier, 1976; Tommasi et al., 1999, 2000). Orthopyroxene CPOs indicate deformation with dominant activation of the (100)[001] slip system. They are always correlated to the olivine CPO, implying that they record the same deformation event.

Textural evidence for metasomatism in these rocks encompasses: (1) small interstitial orthopyroxene grains, (2) small interstitial clinopyroxene grains, (3) the anhedral shapes of some larger pyroxenes, (4) common olivine inclusions in orthopyroxenes, (5) interpenetrating olivine and orthopyroxene grain boundaries. Observations (1), (3), and (4) suggest secondary crystallization of orthopyroxene, while observation (2) indicates secondary crystallization of clinopyroxene. Observation (5) may result from olivine crystallization at the expenses of orthopyroxene as a result of interaction with Si-undersaturated melts or from orthopyroxene crystallization at the expenses of olivine in response to reactions with Si-rich fluids or melts. Interstitial orthopyroxenes and clinopyroxenes sometimes display intracrystalline deformation features. Moreover, pyroxenes CPOs are usually coherent with the olivine one, suggesting that the metasomatic event(s) responsible for their crystallization was pre- to syn-kinematic. Based on geochemical analyses, Bedini et al. (1997) identified two distinct types of metasomatism among those rocks (see section 2.2 for more details). The geochemical characteristics of M1 peridotites were interpreted as the result of interaction with small fractions of LILE-enriched melts saturated in Ti-oxides, whereas M2 peridotites are believed to have re-equilibrated with high fractions of basaltic melts. Using numerical simulation of reactive porous flow at the transition between the lithospheric and the convective mantle, they demonstrated that the processes responsible for the two metasomatisms could be contemporary and linked to thermo-mechanical erosion of the lower lithosphere above a mantle plume. Despite the fact that they equilibrated with different melt fractions, we do not observe any significant variation of the peridotites' microstructures, contrary to what Bedini et al. (1997) pointed out, suggesting pre- or syn-kinematic rather than post-kinematic metasomatism. In their simulation, a series of distinct reactions occurs in a single melt percolation column. Melt-peridotite reactions at the top of the percolation column allow crystallization of clinopyroxene from the consumption orthopyroxene, whereas the two reactions at the bottom crystallize orthopyroxene at the expenses of olivine or olivine at the expense of orthopyroxene. While crystallization of orthopyroxene at the expense of olivine might be suggested by observation (4), we found no evidence for clinopyroxene crystallization at the expense of orthopyroxene in these rocks. The pyroxenites from southern Mega were interpreted by Bedini (1994) as magmatic conduits formed during the same

metasomatic event that originated in the two types of metasomatism identified in peridotites. The fact that some of these pyroxenites exhibit intracrystalline deformation features as well as

pyroxene CPOs reinforces the idea that deformation and metasomatism were at least simultaneous.

*5.2 Anisotropy in the lithospheric mantle beneath the Ethiopian rift*

Our results show that the lithospheric mantle beneath the southern part of the main Ethiopian rift is anisotropic. Calculated maximum seismic anisotropies range between 3.1 and 12.3% for P-waves, and between 2.9 and 8.3 % for S-waves. Estimates for crustal and lithospheric thickness beneath the Ethiopian rift from shear velocity models range between 25-35 km, and 70-80 km, respectively (Dugda et al., 2007). Upper mantle S-wave velocities measured in the region average 4.1-4.2 km/s (Dugda et al., 2007). Along the Main Ethiopian Rift, fast polarization directions slightly oblique to parallel to the rift axis are measured by SKS studies (Kendall et al., 2005). Such orientations are expected for a narrow rift formed as a result of transtension and would result in a near vertical foliation and a near horizontal lineation (Vauchez et al., 2000). In such a case, SKS-waves will then sample the maximum S-wave polarization anisotropy (Z structural direction), leading to delay times ranging between 0.3-0.9s for a 45 km-thick mantle. Higher SKS delay times of 1-3s were measured in the Main Ethiopian Rift, north of the area sampled by the present study (Kendall et al., 2005). In Northern Kenya, south of the study area, slightly lower SKS delay times of 0.8-2.4s have been measured (Gao et al., 1997). Therefore, the anisotropy calculated for the Ethiopian peridotites cannot explain alone the SKS delay times measured within the rift in neighboring regions. This result may indicate that the anisotropic signal is indeed dominated by oriented melt pockets (Ayele et al., 2004; Kendall et al., 2005).

*5.3 Consequences for the deformation of the lithospheric mantle beneath a continental rift*

The microstructures and the relations between magma percolation and deformation we observe in the xenoliths from Mega are different from those observed in other xenolith localities along the East African rift, in the North Tanzanian Divergence and the Masarbit volcanic field in Northern Kenya.

The apparent homogeneity of the microstructures and CPOs of the xenoliths from South Mega suggests that they were acquired during a single deformation event that occurred during the metasomatic event that led to the refertilisation of these rocks, probably the one

interpreted in geochemical studies as the result of interaction with a plume head (Bedini et al., 1997). In Ethiopia, the rapid formation of the magmatic Plateau during a plume-related peak volcanism at 30 Ma (Ebinger, 1993; Georges et al., 1998; Hofman et al., 1997) was followed in the Miocene by continental extension initiation and a volcanic episode also interpreted as plume-related (Ebinger et al., 1993; Hendrie et al. 1994; Morley et al. 1992). Therefore, we expect the deformation recorded by the xenoliths from South Mega to be rift-related. The relatively weak annealing of these samples and the high equilibrium temperatures of samples devoid of exsolutions in orthopyroxene suggest that they were deformed not long before extraction. Common exsolutions in orthopyroxenes suggest the region underwent a later cooling.

Previous studies have described the microstructures and CPOs in mantle xenoliths from other localities of the East African rift. In the Masarbit volcanic field in Northern Kenya (in the Anza Graben), the porphyroclastic to ultramylonitic microstructures suggest intense deformation and strain localisation. Based on thermobarometry and geochemistry measurements and textural analysis, Kaeser et al. (2006) suggested that these deformation was linked to the exhumation of subcontinental mantle lithosphere during the early stages of continental rifting. Deformation and decompression was then followed by a heating and melt infiltration event (Kaeser et al., 2006). In mylonites, olivine CPOs are coherent with deformation with activation of [001](010) slip system (Kaczmarek and Reddy, 2013). In the North Tanzanian Divergence, the microstructure of rift axis peridotites mainly ranges from mylonitic to porphyroclastic and shows evidence for melt-assisted deformation (Baptiste et al., submitted). Olivine CPOs range from axial-[100] to orthorhombic (Fig. 4; Baptiste et al., submitted). The microstructures of the xenoliths from Southern Mega are more homogeneous then these localities. Mylonites or fine-grained porphyroclastic structures, indicating deformation under high stress conditions are not observed. All these observations form various xenolith localities of the East African rift suggest that, although melt infiltration within the lithospheric mantle seems to be a common process along the East African Rift, its timing relative to the beginning of the deformation and the resulting microstructures vary from a region to another.

**Conclusion**

The peridotites from South Mega in the East African rift display homogeneous microstructures, suggesting that they probably do no record any spatial nor temporal variations of deformations conditions. We do not observe any significant change in

microstructures with the geochemical group, despite what was previously reported by Bedini et al. (1997). Slight variations in subgrain boundary spacing in olivine porphyroclasts and in polygonization among olivine neoblast however suggest that the deformation was followed by variable annealing. Exsolutions in pyroxenes indicate later cooling. The orthorhombic olivine CPOs indicate deformation by dislocation creep with dominant activation of the [100] (010) slip system. Evidence for interstitial orthopyroxene and clinopyroxene suggest secondary crystallisation, probably associated to a single metasomatic event identified by Bedini et al. (1997). The CPOs observed in orthopyroxene and sometimes in clinopyroxene, as well as the coherence between olivine and orthopyroxene CPOs in most pyroxenes indicate that metasomatism was pre- to syn-kinematic. Pyroxenites display granular to porphyroclastic microstructures and weaker CPO patterns, suggesting pre- to syn-kinematic metasomatism. Calculated maximum seismic anisotropies range between 3.1 and 12.3% for P-waves, and between 2.9 and 8.3 % for S-waves. These anisotropies cannot explain alone the SKS delay times measured in the main Ethiopian rift or in the Kenya rift. Variations in microstructures and relations between magma percolation and deformation in Ethiopian peridotites are different to what is observed in other xenoliths localities from the East African rift. This indicates that, although melt infiltration within the lithospheric mantle during rifting is commonly observed, its timing relative to deformation and the resulting microstructures varies.

**Acknowledgements**

D. Mainprice provided the programs for calculating seismic properties. C. Nevado and D. Delmas prepared high-quality polished thin sections for FTIR and EBSD measurements. EBSD analyses were performed with the help of F. Barou at the EBSD-SEM national facility at Geosciences Montpellier.